17. Tan, Y., Hanin, L.: Handbook of Cancer Models with Applications. Series in Mathematical Biology and Medicine. World Scientific, Singapore (2008)
18. Deisboeck, T.S., Stmatakos, S.: Multiscale Cancer Modeling. Mathematical and Computational Biology Series. CRC/Taylor and Francis Group, Boca Raton (2011)
19. Wodarz, D., Komarova, N.L.: Computational Biology of Cancer. Lecture Notes and Mathematical Modeling. World Scientific, Hackensack (2005)
20. Astanin, S., Preziosi, L.: Multiphase models of tumor growth. In: Selected Topics in Cancer Modeling. Modeling and Simulation in Science, Engineering, and Technology, pp. 1–31. Birkhäuser, Boston (2008)
21. Wise, S.M., Lowngrub, J.S., Frieboes, H.B., Cristini, V.: Three-dimensional multispecies nonlinear tumor growth-I model and numerical method. J. Theor. Biol. **253**, 524–543 (2008)
22. Travasso, R.D.M., Castro, M., Oliveira, J.C.R.E.: The phase-field model in tumor growth. Philos. Mag. **91**(1), 183–206 (2011)
23. Travasso, R.D.M., Poire, E.C., Castro, M., Rodrguez, J.C.M.: Tumor angiogenesis and vascular patterning: a mathematical model. PLos One **6**(5), 1–9 (2011)
24. Taylor, C.A., Hughes, J.T.R., Zarins, C.K.: Finite element modeling of blood flow in arteries. Comput. Methods Appl. Mech. Eng. **158**, 155–196 (1998)
25. Tang, B.T., Fonte, T.A., Chan, F.P., Tsao, P.S., Feinstein, J.A., Taylor, C.A.: Three dimensional hemodynamics in the human pulmonary arteries under resting and exercise conditions. Ann. Biomed. Eng. **39**(1), 347–358 (2011)

Medical Imaging

Charles L. Epstein
Departments of Mathematics and Radiology,
University of Pennsylvania, Philadelphia, PA, USA

Synonyms

Magnetic resonance imaging; Radiological imaging; Ultrasound; X-ray computed tomography

Description

Medical imaging is a collection of technologies for noninvasively investigating the internal anatomy and physiology of living creatures. The prehistory of modern imaging includes various techniques for physical examination, which employ palpation and other external observations. Though the observations are indirect and require considerable interpretation to relate to the internal state of being, each of these methods is based on the principle that some observable feature differs between healthy and sick subjects. While new technologies have vastly expanded the collection of available measurements, this basic principle remains the central tenet of medical imaging.

Modern medical imaging is divided into different modalities according to the physical principles underlying the measurement process. These differences in underlying physics lead to contrasts in the images that reflect different aspects of anatomy or physiology. The utility of a modality is largely governed by three interconnected considerations: contrast, resolution, and noise. Contrast refers to the physical or chemical distinctions that produce the image itself, and the magnitude of these differences in the reconstructed image. Resolution is usually thought of as the size of the smallest objects discernible in the image. Finally noise is an inevitable consequence of real physical measurements. The ratio between the size of the signal and the size of the noise which contaminates it, called SNR, limits both the contrast and resolution attainable in any reconstructed image.

Technological advances in the nineteenth and twentieth centuries led to a proliferation of methods for medical imaging. The first such advances were the development of photographic imaging, and the discovery of x-rays. These were the precursors of projection x-rays, which led, after the development of far more sensitive solid-state detectors, to x-ray tomography. Sonar, which was used by the military to detect submarines, was adapted, along with ideas from radar, to ultrasound imaging. In this modality high-frequency acoustic energy is used as a probe of internal anatomy. Taking advantage of the Döppler effect, ultrasound can also be used to visualize blood flow, see [7].

Nuclear magnetic resonance, which depends on the subtle quantum mechanical phenomenon of spin, was originally developed as a spectroscopic technique in physical chemistry. With the advent of powerful, large, high-quality superconducting magnets, it became feasible to use this phenomenon to study both internal anatomy and physiology. In its simplest form the contrast in MRI comes from the distribution of water molecules within the body. The richness of the spin-resonance phenomenon allows the use of other experimental protocols to modulate the contrast, probing

many aspects of the chemical and physical environment.

The four imaging modalities in common clinical use are (1) x-ray computed tomography (x-ray CT), (2) ultrasound (US), (3) magnetic resonance imaging (MRI), and (4) emission tomography (PET and SPECT). In this article we only consider the details of x-ray CT and MRI. Good general references for the physical principles underlying these modalities are [4, 7].

There are also several experimental techniques, such as diffuse optical tomography (DOT) and electrical impedance tomography (EIT), which, largely due to intrinsic mathematical difficulties, have yet to produce useful diagnostic tools. A very promising recent development involves hybrid modalities, which combine a high-contrast (low-resolution) modality with a high-resolution (low-contrast) modality. For example, photo-acoustic imaging uses infrared light for excitation of acoustic vibrations and ultrasound for detection, see [1].

Each measurement process is described by a mathematical model, which in turn is used to "invert" the measurements and build an image of some aspect of the internal state of the organism. The success of an imaging modality relies upon having a stable and accurate inverse algorithm, usually based on an exact inversion formula, as well as the availability of sufficiently many measurements with an adequate signal-to-noise ratio. The quality of the reconstructed image is determined by complicated interactions among the size and quality of the data set, the available contrast, and the inversion method.

X-Ray Computed Tomography

The first "modern" imaging method was the projection x-ray, introduced in the late 1800s by Roentgen. X-rays are a high-energy form of electromagnetic radiation, which pass relatively easily through the materials commonly found in living organisms. The interaction of x-rays with an object B is modeled by a function $\rho_B(\mathbf{x})$, called the *attenuation coefficient*. Here $\mathbf{x}$ is a location within B. If we imagine that an x-ray beam travels along a straight line, ℓ, then Beer's law predicts that $I(s)$, the intensity of the beam satisfies the differential equation:

$$\frac{dI}{ds} = -\rho_B(\mathbf{x}(s))I(s). \tag{1}$$

Medical Imaging, Fig. 1 A projection x-ray image (Image courtesy: Dr. Ari D. Goldberg)

Here $\mathbf{x}(s)$ is the point along the line, ℓ, and s is arc-length parametrization. If the intersection $\ell \cap B$ lies between $s_{\min}$ and $s_{\max}$, then Beer's law predicts that:

$$\log\left(\frac{I_{\text{out}}}{I_{\text{in}}}\right)(\ell) = -\int_{s_{\min}}^{s_{\max}} \rho_B(\mathbf{x}(s))ds. \tag{2}$$

Early x-ray images recorded the differential attenuation of the x-ray beams by different parts of the body, as differing densities on a photographic plate. In the photograph highly attenuating regions appear light, and less dense regions appear dark. An example is shown in Fig. 1. X-ray images display a good contrast between bone and soft tissues, though there is little contrast between different types of soft tissues. While the mathematical model embodied in Beer's law is not needed to interpret projection x-ray images, it is an essential step to go from this simple modality to x-ray computed tomography.

X-ray CT was first developed by Alan Cormack in the early 1960s, though the lack of powerful computers made the idea impractical. It was rediscovered by Godfrey Hounsfield in the early 1970s. Both received the Nobel prize for this work in 1979, see [6]. Hounsfield was inspired by the recent development of solid-state x-ray detectors, which were more sensitive and had a much larger dynamic range than photographic film. This is essential for medical applications of x-ray CT, as the attenuation coefficients of different soft tissues in the human body differ by less than 3 %. By 1971, solid-state detectors and improved computers made x-ray tomography a practical possibility.

The mathematical model embodied in Beer's law leads to a simple description of the measurements available in an x-ray CT-machine. Assuming that we have a monochromatic source of x-rays the measurement described in (2) is the Radon (in two dimensions), or x-ray transform (in three dimensions) of the attenuation coefficient, $\rho_B(\mathbf{x})$. For simplicity we consider the two-dimensional case.

The collection, $\mathcal{L}$, of oriented lines in $\mathbf{R^2}$ is conveniently parameterized by $S^1 \times \mathbf{R^1}$, with (t, θ) corresponding to the oriented line:

$$\ell_{t,\theta} = \{t(\cos\theta, \sin\theta) + s(-\sin\theta, \cos\theta) : \ s \in \mathbf{R^1}\}. \tag{3}$$

The Radon transform can then be defined by:

$$\mathcal{R}\rho_B(t,\theta) = \int_{\ell_{t,\theta}} \rho_B(t(\cos\theta, \sin\theta) + s(-\sin\theta, \cos\theta))ds. \tag{4}$$

The measurements made by an x-ray CT-machine are modeled as samples of $\mathcal{R}\rho_B(t,\theta)$. The actual physical design of the machine determines exactly which samples are collected. The raw data collected by an x-ray CT-machine can be represented as a sinogram, as shown in Fig. 2. The reconstructed image is shown in Fig. 3.

The inversion formula for the Radon transform is called the *filtered back-projection* formula. It is derived by using the Central Slice theorem:

Theorem 1 (Central Slice Theorem) *The Radon transform of ρ, $\mathcal{R}\rho$, is related to its two-dimensional Fourier transform, $\mathcal{F}\rho$, by the one-dimensional Fourier transform of $\mathcal{R}\rho$ in t :*

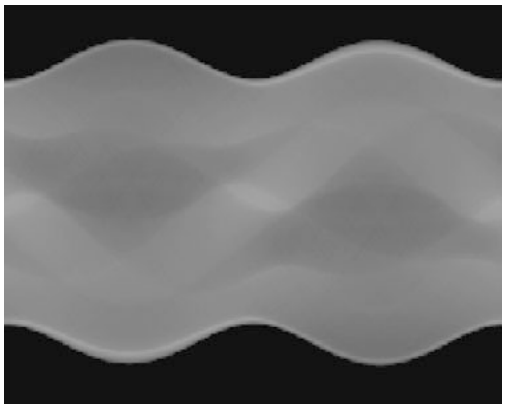

Medical Imaging, Fig. 2 Radon transform data, shown as a sinogram, for the Shepp–Logan phantom. The horizontal axis is θ and the vertical axis t

Medical Imaging, Fig. 3 Filtered back-projection reconstruction of the Shepp–Logan phantom from the data in Fig. 2

$$\widetilde{\mathcal{R}\rho}(\tau,\theta) = \int_{-\infty}^{\infty} \mathcal{R}\rho(t,\theta)e^{-it\tau}dt = \mathcal{F}\rho(\tau(\cos\theta, \sin\theta)). \tag{5}$$

This theorem and the inversion formula for the two-dimensional Fourier transform show that we can reconstruct ρ_B by first filtering the Radon transform:

$$\mathcal{G}\mathcal{R}\rho_B(\tau,\theta) = \frac{1}{2\pi}\int_{-\infty}^{\infty} \widetilde{\mathcal{R}\rho_B}(r,\theta)e^{ir\tau}|r|dr. \tag{6}$$

M

and then back-projecting, which is $\mathcal{R}^*$, the adjoint of the Radon transform itself:

$$\rho_B(x,y)=\frac{1}{2\pi}\int_0^\pi \mathcal{G}\mathcal{R}\rho_B(\langle(\cos\theta,\sin\theta),(x,y)\rangle,\theta)d\theta. \tag{7}$$

The filtration step $\mathcal{R}\rho_B \rightarrow \mathcal{G}\mathcal{R}\rho_B$ is implemented using a fast Fourier transform. The multiplication by $|r|$ in the frequency domain makes it mildly ill-conditioned; nonetheless the high quality of the data available in a modern CT-scanner allows for stable reconstructions with a resolution of less than a millimeter. As a map from a function $g(t,\theta)$ on $\mathcal{L}$ to functions on $\mathbf{R^2}$, back-projection can be understood as half the average of g on the set of lines that pass through (x,y). A detailed discussion of x-ray CT can be found in [2].

Magnetic Resonance Imaging

Magnetic resonance imaging takes advantage of the fact that the protons in water molecules have both an intrinsic magnetic moment μ and an intrinsic angular momentum, $\mathbf{J}$, known as spin. As both of these quantum mechanical observables transform by the standard representation of $SO(3)$ on $\mathbf{R^3}$, the Wigner–Eckert Theorem implies that there is a constant γ, called the gyromagnetic ratio, so that $\mu=\gamma\mathbf{J}$. For a water proton $\gamma \approx 42.5\,\text{MHz/T}$. If an ensemble of water protons is placed in a static magnetic field $\mathbf{B_0}$, then, after a short time, the protons become polarized producing a bulk magnetization $\mathbf{M}_0$. If $\rho(\mathbf{x})$ now represents the density of water, as a function of position, then thermodynamic considerations show that there is a constant C for which:

$$\mathbf{M}_0(\mathbf{x}) \approx \frac{C\rho(\mathbf{x})}{T}\mathbf{B_0}(\mathbf{x}). \tag{8}$$

At room temperature ($T \approx 300°\text{K}$) this field is quite small and is, for all intents and purposes, not *directly* detectable.

A clinical MRI scanner consists of a large solenoidal magnet, which produces a strong, homogeneous background field, $\mathbf{B_0}$, along with coaxial electromagnets, which produce gradient fields $\mathbf{G(t)}\cdot\mathbf{x}$, used for spatial encoding, and finally a radio-frequency (RF) coil, which produces an excitation field, $\mathbf{B_1(t)}$, and is also used for signal detection.

The total magnetic field is therefore: $\mathbf{B(x,t)} = \mathbf{B_0(x)} + \mathbf{G(t)}\cdot\mathbf{x} + \mathbf{B_1(t)}$. The response of the bulk nuclear magnetization, $\mathbf{M}$, to such a field is governed by Bloch's phenomenological equation:

$$\frac{d\mathbf{M}}{dt}(\mathbf{x},t) = \gamma\mathbf{M}(\mathbf{x},t)\times\mathbf{B}(\mathbf{x},\mathbf{t}) - \left(\frac{\mathbf{1}}{\mathbf{T_1(x)}}\right) (\mathbf{M}^{\|}(\mathbf{x},t) - \mathbf{M}_0(\mathbf{x})) - \left(\frac{1}{T_2(\mathbf{x})}\right)\mathbf{M}^{\perp}(\mathbf{x},t). \tag{9}$$

Here $\mathbf{M}^{\|}$ is the component of $\mathbf{M}$ parallel to $\mathbf{B_0}$ and $\mathbf{M}^{\perp}$ is the orthogonal component. The terms with coefficients T_1 and T_2 describe relaxation processes which tend to relax $\mathbf{M}$ toward the equilibrium state $\mathbf{M}_0$. The components $\mathbf{M}^{\|}$ and $\mathbf{M}^{\perp}$ relax at different rates $T_1 > T_2$. In most medical applications their values lie in the range of 50 ms–2 s. The spatial dependence of T_1 and T_2 provides several possibilities for contrast in MR-images, sometimes called T_1- or T_2-weighted images. Note that (9) is a system of ordinary differential equations in time, t, and that the spatial position, $\mathbf{x}$, appears as a pure parameter.

Ignoring the relaxation terms for the moment and assuming that $\mathbf{B}$ is independent of time, we see that (9) predicts that the magnetization $\mathbf{M(x)}$ will precess around the $\mathbf{B_0(x)}$ with angular velocity $\omega=\gamma\|\mathbf{B_0(x)}\|$. This is the *resonance* phenomenon alluded to in the name "nuclear magnetic resonance." Faraday's Law predicts that such a precessing magnetization will produce an E.M.F. in a coil C with

$$\mathcal{EMF} \propto \frac{d}{dt}\int_\Sigma \mathbf{M}(\mathbf{x},t)\cdot\mathbf{n}(\mathbf{x})\mathbf{dS}, \tag{10}$$

for Σ a surface spanning C. A simple calculation shows that the strength of the signal is proportional to ω^2, which explains the utility of using a very strong background field. The noise magnitude in MR-measurements is proportional to ω, hence the SNR is proportional to ω as well.

For the remainder of this discussion we assume that $\mathbf{B_0}$ is a homogeneous field of the form $\mathbf{B_0} = (\mathbf{0},\mathbf{0},\mathbf{b_0})$. The frequency $\omega_0=\gamma b_0$ is called the Larmor frequency. The main magnet of a clinical scanner typically has a field strength between 1.5 and 7 T, which translates to Larmor frequencies between 64 and 300 MHz.

The RF-component of the field $\mathbf{B_1(t)}$ is assumed to take the form:

$$(a(t)\cos\omega_0 t, a(t)\sin\omega_0 t, 0),$$

with $a(t)$ nonzero for a short period of time. As implied by the notation, the gradient fields are designed to have a linear spatial dependence, and therefore take the form:

$$\mathbf{G(t)}\cdot\mathbf{x} = (\mathbf{g_1(t)x_3} - \mathbf{g_3(t)x_1}, \mathbf{g_2(t)x_3}, \mathbf{g_1(t)x_1} + \mathbf{g_2(t)x_2} + \mathbf{g_3(t)x_3}). \quad (11)$$

Here $\mathbf{g(t)} = (\mathbf{g_1(t)}, \mathbf{g_2(t)}, \mathbf{g_3(t)})$ is a spatially independent vector describing the time course of the gradient field. Typically $\|\mathbf{g}\| << \mathbf{b_0}$, which allows us to ignore components of $\mathbf{G}$ orthogonal to $\mathbf{B_0}$.

Assume that the object modeled by $\rho(\mathbf{x})$ lies in a region $[-L, L]\times[-L, L]\times[-L, L]$. Allowing the spins to become polarized creates a bulk magnetization $\mathbf{M}_0$ parallel to $\mathbf{B_0}$, see (8). As noted $\mathbf{M}_0$ is a tiny field, which is essentially undetectable. An RF-field is then turned on for a short period of time, usually in the presence of a gradient field. At the end of this so-called *selective excitation*, Bloch's equation predicts that the field $\mathbf{M(x)}$ remains in the equilibrium position for $x_3 \notin [a, b]$, whereas for $x_3 \in [a, b]$, $\mathbf{M(x)}$ now has a nontrivial $\mathbf{M}^{\perp}$-component, which precesses producing a measurable signal. With a, possibly different, gradient field turned on, the measured signal takes the form:

$$s(t) \propto \omega_0^2 e^{i\omega_0 t} \int_{-L}^{L}\int_{-L}^{L}\int_{a}^{b} \rho(x_1, x_2, x_3)\, e^{-it\gamma(g_1x_1+g_2x_2)}\, dx_3 dx_1 dx_2. \quad (12)$$

The integral is the two-dimensional Fourier transform, $\mathcal{F}\overline{\rho}(k_1, k_2)$, at spatial frequency $(k_1, k_2) = t\gamma(g_1, g_2)$, of the averaged spin-density:

$$\overline{\rho}(x_1, x_2) = \int_a^b \rho(x_1, x_2, x_3)\, dx_3. \quad (13)$$

The *slice thickness*, $|b - a|$, is typically several millimeters. By sampling in time and repeating this process with different gradients (g_1, g_2), we can obtain samples of $\mathcal{F}\overline{\rho}$ for frequencies in a neighborhood of $(0, 0)$. The extent of this neighborhood determines the maximum resolution available in the reconstructed image.

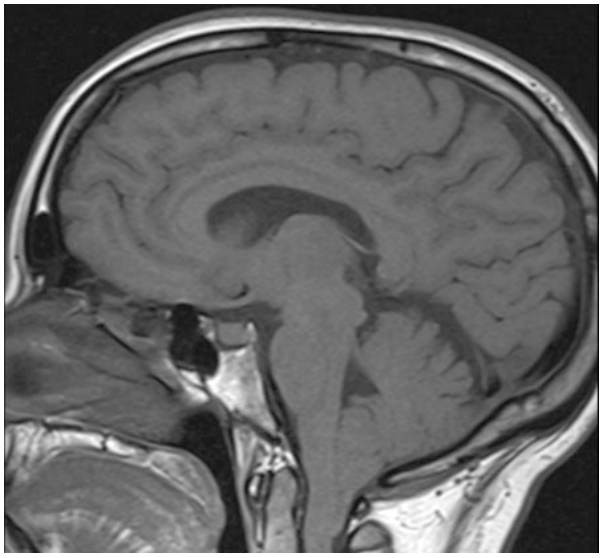

Medical Imaging, Fig. 4 A T1-weighted, spin-echo MR-image of the brain, made on a scanner with 3 T magnet. The slice thickness ($|b - a|$ in (13)) is 3 mm (Image courtesy of Dr. Ari D. Goldberg)

The reconstruction formula for MRI is simply the inverse Fourier transform:

$$\overline{\rho}(x_1, x_2) = \frac{1}{4\pi^2}\int_{-\infty}^{\infty}\int_{-\infty}^{\infty} \mathcal{F}\overline{\rho}(k_1, k_2) e^{i(k_1x_1+k_2x_2)}\, dk_1 dk_2. \quad (14)$$

As a unitary map it is intrinsically stable and very accurately approximated by the discrete Fourier transform. The main limitation in MR-imaging is noise, which is controlled by repeated acquisition and signal averaging. Using data acquired in approximately 10 min, a low-noise image of the brain with an in-plane resolution of approximately 1 mm can be reconstructed, see Fig. 4. For more on magnetic resonance imaging see [3, 5].

References

1. Ammari, H.: An Introduction to Mathematics of Emerging Biomedical Imaging. Mathématiques & Applications (Berlin) [Mathematics & Applications], vol. 62. Springer, Berlin (2008)

2. Epstein, C.L.: Introduction to the Mathematics of Medical Imaging, 2nd edn. Society for Industrial and Applied Mathematics (SIAM), Philadelphia (2008)
3. Haacke, E.M., Brown, R.W., Thompson, M.R., Venkatesan, R.: Magnetic Resonance Imaging. Wiley-Liss, New York (1999)
4. Kak, A., Slaney, M.: Principles of Computerized Tomographic Imaging. Classics in applied mathematics, vol. 33, 327p. Society for Industrial and Applied Mathematics, Philadelphia (2001)
5. Liang, Z.P., Lauterber, P.C.: Principles of Magnetic Resonance Imaging: A Signal Processing Perspective. Series in Biomedical Engineering. Wiley–IEEE Press, New York (2000)
6. Nobel: http://nobelprize.org/nobelorganizations/nobelfoundation/publications/lectures/index.html (1979)
7. Suetens, P.: Fundamentals of Medical Imaging, 2nd edn. Cambridge University Press, Cambridge, New York (2009)

Meshless and Meshfree Methods

Jiun-Shyan Chen[1] and Ted Belytschko[2]
[1]Department of Structural Engineering, University of California, San Diego, CA, USA
[2]Department of Mechanical Engineering, Northwestern University, Evanston, IL, USA

Introduction

Finite difference method (FDM) and finite element method (FEM) rely on a mesh (or stencil) to construct the local approximation of functions and their derivatives for solving partial differential equations (PDEs). A few drawbacks are commonly encountered in these methods: (1) time consuming in generating good quality mesh in arbitrary geometry for desired accuracy; (2) difficult in constructing approximations with arbitrary order of continuity, making the solution of PDE with higher-order differentiation or problems with discontinuities difficult to solve; (3) tedious in performing h- or p-adaptive refinement; and (4) ineffective in dealing with mesh entanglement-related difficulties (such as those in large deformation and fragment-impact problems), among others.

The origin of meshfree methods (also called meshless methods) can be traced back to the generalized finite difference method [38, 54] and the smoothed particle hydrodynamics (SPH) [24, 56], in which the approximation of a function and its derivatives were constructed based on a set of points that are not interconnected in the traditional sense. In the past 20 years, meshfree methods have emerged into a new class of computational methods with considerable success. Meshfree methods all share a common feature: the approximation of unknowns in the PDE is constructed based on scattered points without mesh connectivity. As shown in Fig. 1, the approximation function at point I in FEM is constructed from the element level natural coordinate and then transformed to the global Cartesian coordinate, whereas the meshfree approximation functions are constructed using only nodal coordinate data at the global Cartesian coordinate directly. These compactly supported meshfree approximation functions form a partition of unity subordinated to the open covering with controllable orders of continuity and completeness. It becomes possible to relax the strong tie between the quality of discretization and the quality of approximation in FEM with this class of approximation functions, and it significantly simplifies the procedures in h-adaptivity. Special basis functions can be embedded in the approximation to capture essential characteristics in the approximated functions, and arbitrary discontinuities can be introduced in the approximation as well. This entry gives an overview of several classes of meshfree approximation functions and presents how these meshfree approximation functions can be used to solve PDEs.

Function Approximation by a Set of Scattered Points

Moving Least-Squares Approximation (MLS)

Let the domain of interest $\bar{\Omega} = \Omega \cup \partial\Omega$ be discretized by a set of points $S = \{\boldsymbol{x}_1 \dots \boldsymbol{x}_{N_p} | \boldsymbol{x}_I \in \bar{\Omega}\}$ with corresponding point numbers that form a set $Z_S = \{I | \boldsymbol{x}_I \in S\}$. The weighted local approximation of a set of sample data $\{(\boldsymbol{x}_I, u_I)\}_{I \in Z_S}$ near $\bar{\boldsymbol{x}}$, denoted by $u^h_{\bar{\boldsymbol{x}}}(\boldsymbol{x})$, is expressed as

$$u^h_{\bar{\boldsymbol{x}}}(\boldsymbol{x}) = \sum_{i=1}^{n} p_i(\boldsymbol{x}) b_i(\bar{\boldsymbol{x}}) = \boldsymbol{p}^T(\boldsymbol{x}) \boldsymbol{b}(\bar{\boldsymbol{x}}) \qquad (1)$$

where $\{p_i(\boldsymbol{x})\}_{i=1}^n$ are the basis functions and $\{b_i(\bar{\boldsymbol{x}})\}_{i=1}^n$ are the corresponding coefficients that are functions of local position $\bar{\boldsymbol{x}}$. The coefficients